Schewe, Günter, and Mai, Holger. „Influence of Flexibility on the steady aeroelastic Behavior of a swept Wing in transonic Flow."
Journal of Fluids and Structures **(2018) , 81, pp. 255-269. http://doi.org/10.1016/j.jfluidstructs.2018.04.021**
Postprint:

Influence of Flexibility on the steady aeroelastic Behaviour of a swept Wing in transonic Flow

Günter Schewe & Holger Mai
DLR-Institute of Aeroelasticity, Göttingen, Germany

The development in the last decades generally shows that large aircraft wings have become more light and flexible, thus the investigation of the effects of elasticity is suggested. If for example the flexible wing is also backward swept, then the situation becomes even more complex - the kinematic coupling between bending and torsion leads to a structural washout effect.
In order to investigate the influence of flexibility, in the project "Aerostabil" an aeroelastically scaled half-model was tested compared to its rigid equivalent. The flexible model was equipped with pressure transducers in three wing sections and accelerometers, while the rigid model had a reduced number of sensors. The experiments were performed in the adaptive test section of a transonic wind tunnel. Steady and unsteady pressure-, and force measurements were conducted for fixed and oscillating wings.
Already Dietz et al. (2003) have reported about the special features of the wing models, their structural properties and preliminary results.
The present paper is focused on the analysis of the global forces and pressure distributions for the range $0.5 \leq Ma \leq 0.88$. The angle of attack was varied from -4° to 4° and also the quasistatic aeroelastic derivatives for lift and moment were obtained.
When the model is rigid in the transonic regime and at moderate angles of incidence the pressure distribution exhibits a single shock system, in contrast for the flexible wing there is a double shock system. For the flexible wing up to about Ma = 0.82 the curves of global lift, moment and their derivatives are rather smooth and are remaining on nearly the same level. Beyond there are moderate deviations up to the end of the transonic regime. However examining the corresponding curves of the rigid wing the changes are drastic, particularly in the transonic range. Obviously the structural wash-out, particularly of the outer wing leads to an attenuation of the transonic effects.

Keywords: Transonic Flow; swept Wing; Influence of Flexibility; Aerostabil wing; structural washout effect

1. Introduction

In the last decades the general trend shows that large aircraft wings have become more light and flexible, thus the investigation of the effects of elasticity is even more suggested. Particularly in the transonic regime the interaction between the shock dynamic, the boundary layer and its separation is a significant source of complex behaviour. If the wing is flexible and in addition backward swept, as in case of a real transport aircraft then the kinematic coupling between bending and torsion leads to a washout-effect i.e. a reduction of the streamwise local angle of attack when the bending of the wing is increased. Hence the static bending and torsional deformations depending on the airloads can have drastic consequences on the global aerodynamic behaviour and therefore on the aeroelastic stability.
The aerodynamic foundations of the swept wing concept were laid by Busemann (1935). He predicted that the compressibility effects are shifted to higher values of the Mach number when the wing is backward swept. The fundamental aeroelastic properties of the swept wing were investigated theoretically by Jordan (1946). He described the occurrence of the mentioned kinematic coupling effects between bending and torsion (washout) and he already predicted the possibility of one degree of freedom flutter of a backward swept wing (see also Försching, 2010).
The fields of steady and unsteady transonic aerodynamics and aeroelasticity are reviewed by Tijdeman and Seebass (1980) and Bendiksen (2011).
An early wind tunnel test with flexible models was performed in a German/French cooperation called "Aeroelastic Model Program (AMP)", (Zingel 1991). Two models were applied; a scaled flexible swept wing with 300 pressure transducers and a dynamically scaled model for flutter tests. Apart from the steady and unsteady pressures also the static wing deformations were measured optically as well as the global steady and unsteady forces using a rigid piezoelectric balance. Only a few results are accessible in Zingel (1991) and Arnold et al. (2009). **Figure 1** shows the AMP-wing in the French transonic wind tunnel S2 in Modane.
The present experiments were performed in the framework of the project "Aerostabil" and the features and details of the wing models and their structural properties are already described by Dietz et al. (2003). In that paper there are also a few results presented concerning static aeroelasticity.
In Bendiksen (2009) several investigations of an Aerostabil-similar wing with an identical planform but different airfoil shape and an Euler CFD-solver are presented. In this paper Bendiksen pointed out that the above mentioned wash-out effect is responsible for a special type of flutter, which he called "High-Altitude Limit Cycle Flutter". An example for this phenomenon will be presented in Schewe & Mai (2019).
Neumann and Mai (2013) investigated experimentally and numerically the dynamic response problem using the same elastic Aerostabil model. Upstream of our elastic swept wing a generic gust was produced by a moving 2D wing, which acted as gust generator. The experiments were compared with numerical simulations leading to result concerning steady and unsteady deflections of the elastic wing and pressure distributions. Finally, the results of simulated transfer functions of the gust generator to the elastic wing are presented in comparison to the measurements.
Stickan et al. (2014) used the Aerostabil data as test cases for their numerical simulation. A Navier Stokes solver (DLR-Tau code) and a linear structural shell model were applied. It turned out that the application of a shell-FE-model is necessary for the correct simulation of the Aerostabil experiments.
Based on the experience gained in the AMP-Program, the Aerostabil-Project was planned. Hence the main aim was to study the steady aeroelastic effects and the LCO-flutter behavior of a generic elastic swept wing. Thus a geometry of low complexity was selected.

Nevertheless the aerodynamic shape is close to the geometry of the outer part of a modern transport aircraft wing. The model had a supercritical airfoil and was equipped with pressure transducers in three wing sections. In addition accelerometers were installed and steady and unsteady pressure measurements were taken. A very stiff mount at the root is a prerequisite for wind tunnel test with flexible wings, thus a rigid piezo balance was applied for the measurement of the steady and unsteady global forces. In order to see directly the influence of elasticity a second but rigid wing-model with the same geometry was applied.
Contrary to the mentioned paper by Dietz et al. (2003) the present investigation is concentrated on the description of the procedures during the Aerostabil-experiments and the evaluation of the data. The time functions of global forces, pressure distributions and accelerations were measured, thus steady and unsteady data for the Mach No range $0.5 \leq Ma \leq 0.88$ are available. The angle of attack was varied between $-4° \leq \alpha \leq 4°$ and also quasistatic aeroelastic derivatives were obtained, which reflect partly the behavior of both different wings regarding special effects in the transonic flow regime.
Flutter experiments were analysed systematically in the transonic Mach number range and the results are presented in Schewe & Mai (2019).

Figure 1 AMP-wing in the French transonic wind tunnel S2 in Modane.

2. Test set-up

As mentioned in the introduction, the features and details of the elastic wing model and their structural properties are described in Dietz et al. (2003) and Stickan et al.(2014). The sketch of the test-setup in **Figure. 2** shows that the swept wing model is mounted on a turntable device. The half-wing model represents the starboard outer part of a supercritical wing of a transport aircraft and was equipped with pressure transducers in three wing sections. In addition accelerometers were installed for getting information about the oscillating wing deflections.
The model can be forced by means of a hydraulic rotation actuator to perform pitch oscillations around the spar axis. Laser triangulators are used to measure the angle of incidence α at the root, related to the spar axis. A rigid piezoelectric platform balance is applied to measure the steady and unsteady global forces at the root of the wing. In this context one has to bear in mind that a stiff balance at the root is the prerequisite for measurements with flexible models (Schewe 2007).

For comparisons a second conventional rigid model was tested which had the same geometry as the flexible model. But the stiff model was equipped with only one pressure

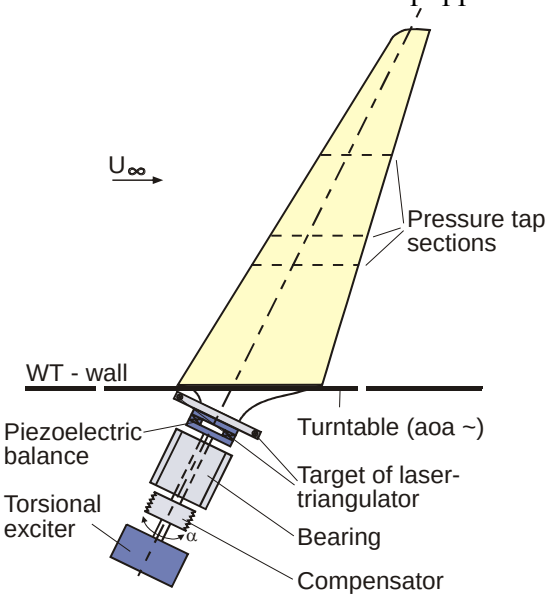

Figure 2 Test setup for oscillating half models in the transonic wind tunnel.

section, whose position corresponds to the spanwise location of the second section of the flexible model, thus a direct comparison is possible.
The laminar/turbulent boundary-layer transition has been tripped during all the tests at 7.5% local chord length at the upper and lower surface. Its effectiveness has been proven by infrared imaging.
Steady and unsteady pressure-, and force measurements were taken for the fixed and oscillating wing. The experiments were performed in the adaptive test section of the transonic wind tunnel in Göttingen (**Figure 3**).
The geometry of the wing model is sketched in **Figure 4**. The aspect ratio including the wing tip amounts to $\lambda = 3.68$. The leading-edge sweepback angle is 32°. The reference chord length of $c^* = 183$ mm and a span without wing tip of $b^* = 600.9$ mm is used for normalization. The wing tip has a width of $\Delta y = 9.4$ mm and its surface has a smooth transition to the wing in a mathematical sense. The wing has a supercritical airfoil and the thickness according to the local chord length remains almost constant along the span with a value of about 10 %.
The construction of the flexible model is as follows: The root of the model consists of a carry-through section made of hardened steel screwed to the piezoelectric balance. The carry-through section extends in a carbon-fiber composite (CFC) spar which is connected to ribs. The aerodynamic surface is shaped by a glass-fiber composite (GFC) skin that is glued to the ribs and the spar. The GFC skin is colored white in order to allow optical deformation measurement technique. The surface has a peak-to-valley surface roughness lower than 20µm.

The instrumentation of the model wing consists of 93 miniature differential pressure transducers Kulite XCQ-093-5psiD in three sections. In three streamwise rows surface pressure orifices are located with diameter of 0.3mm. For measuring vertical motions accelerometers of type PCB 352C22 were applied. Two accelerometers, which are considered in this study are located at $y/c^* = 2.61$ (Fig 1) and one is located near the wing tip at $y/c^* = 3.05$. For getting displacement information, the signals were filtered and then integrated two times.

The signals were scanned with a frequency of f_{scan} = 1.2 kHz and the integration time was T = 16 s. A special flutter test case, which will be presented, was also scanned with the fourfold frequency 4.8kHz.

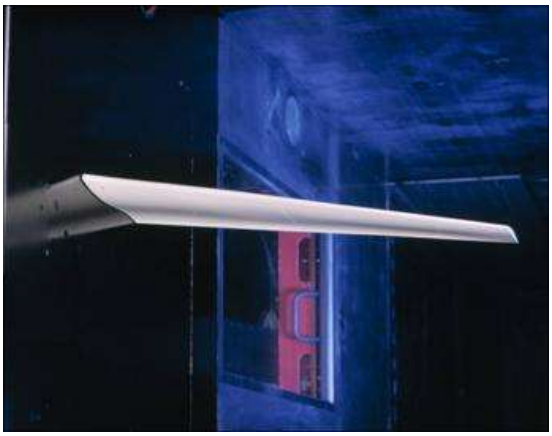

Figure 3. Photo of the Aerostabil wing in the adaptive test section of the transonic wind tunnel in Göttingen.

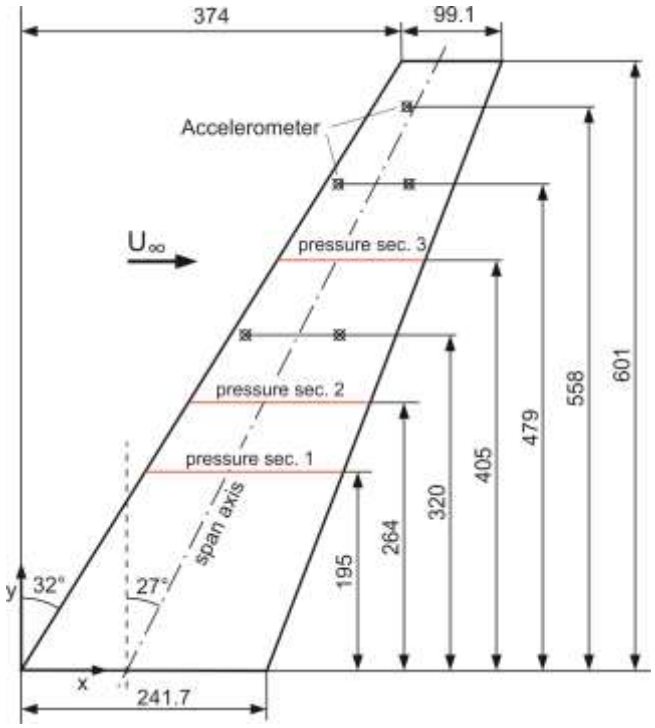

Figure 4 Sketch of Aerostabil geometry, including the three pressure measurement sections and acceleration sensors.

Schewe, Günter, and Mai, Holger. „Influence of Flexibility on the steady aeroelastic Behavior of a swept Wing in transonic Flow."
Journal of Fluids and Structures **(2018) , 81, pp. 255-269. http://doi.org/10.1016/j.jfluidstructs.2018.04.021**

The measured structural properties are described in detail in Dietz et al. (2003). An identification of mode shapes with a high spatial resolution was performed by means of a scanning Laser Doppler Vibrometer (LDV). The first bending mode of the flexible wing without wind has a value of $f_{B1}^* = 37.81$ Hz and a damping of $\delta = 0.52\%$ (second mode: $f_{B2}^* = 112.9$ Hz and a damping of $\delta_B = 0.39\%$. The first torsion mode amounts to $f_{T1}^* = 272.6$ Hz and a damping of $\delta_T = 0.04\%$.
The total mass of the elastic wing attached to the balance was $m^* = 6.602$kg.
The ratio of structural forces to the aerodynamic loads is described by the mass ratio $\mu = (m^* / (\pi / 4 \; c^{*2} \; b^*)) / \rho^*_\infty = 417.68 \; kg/m^3 / \rho^*_\infty$.

The transonic wind tunnel in Göttingen (DNW-TWG) is a continuously working closed-circuit facility with a $1 \times 1 \; m^2$ squared test section. The ratio of the test-section height to the reference chord of the research model amounts to 5.46 and the ratio of spanwidth to wind-tunnel width is 0.6. The top and bottom walls of the wind-tunnel test section were adapted to the steady flow at the mean angle of attack when the aerodynamic loads to the model are in balance to the structural forces and the structure does not oscillate. The wall interference is minimized according to a target-line method for the two-dimensional wall adaptation for three-dimensional flows. The wall shapes are determined from that pressure data by an algorithm developed by Lamarche and Wedemeyer (1984).

The global aerodynamic forces and moments were reduced to aerodynamic coefficients as follows: The reference area is the horizontal projection area of the wing with $A^* = 0.10033 m^2$. The streamwise moment center is located according to the geometrical neutral point of the wing at $x = 1.047$. The spanwise moment center is located at the wind-tunnel wall $y = 0$ while the vertical moment center is chosen to be $z = 0$. The reference area A^* and the reference chord length c^* are used to normalize the global pitching-moment coefficient c_m . The Reynolds number Re is referred to length c^*. In the context of pressure distributions c is the local cord length of the wing.

3. Comparison between flexible and rigid wing

3.1 Global values

The global steady and unsteady forces were measured using the piezoelectric balance at the root of the wing. Even the steady force coefficients and its derivatives reflect partly the behavior of both different wings regarding special effects in the transonic flow regime.
In order to illuminate the individual effects depending on angle of attack, Mach No and mass ratio or Reynolds number in the following figures the resulting data are presented in different representations. In both cases (rigid/flexible model) the Mach No was varied in the range $0.5 \leq Ma \leq 0.88$ and by adapting the tunnel pressure the Reynolds number was held constant around $Re \approx 1.3e6$.
In **Figure 5**. a comparison of the lift coefficient for the rigid model (A) and the flexible model (B) is displayed. For the rigid model at ten Mach numbers a lift curve was taken for angles of attack between $-4° \leq \alpha \leq 4°$ and in steps of 0.5° (left figure) . Using the flexible model at six Mach numbers a lift curve was taken for angles between $-3° \leq \alpha \leq 3°$ and in steps of 0.25° (right figure).
Even at the first glance it is obvious that for the rigid wing the curves become a little bit bended when the Mach No is increasing and it is also evident that the overall slope is varying. Close inspection shows that only at Ma = 0.5 there is a nearly linear line with the smallest slope. For the flexible wing (right figure) however the curves seem to be more or less straight and the variation of the slopes is less, only the curve for Ma = 0.88 is a little bit steeper. For

the low lift case, where the smallest deformation effects can be expected i.e. Ma = 0.5 and α = - 3°, the lift coefficients for both wings is nearly equal c_{l_b}(Ma = 0.5) = 0.1.

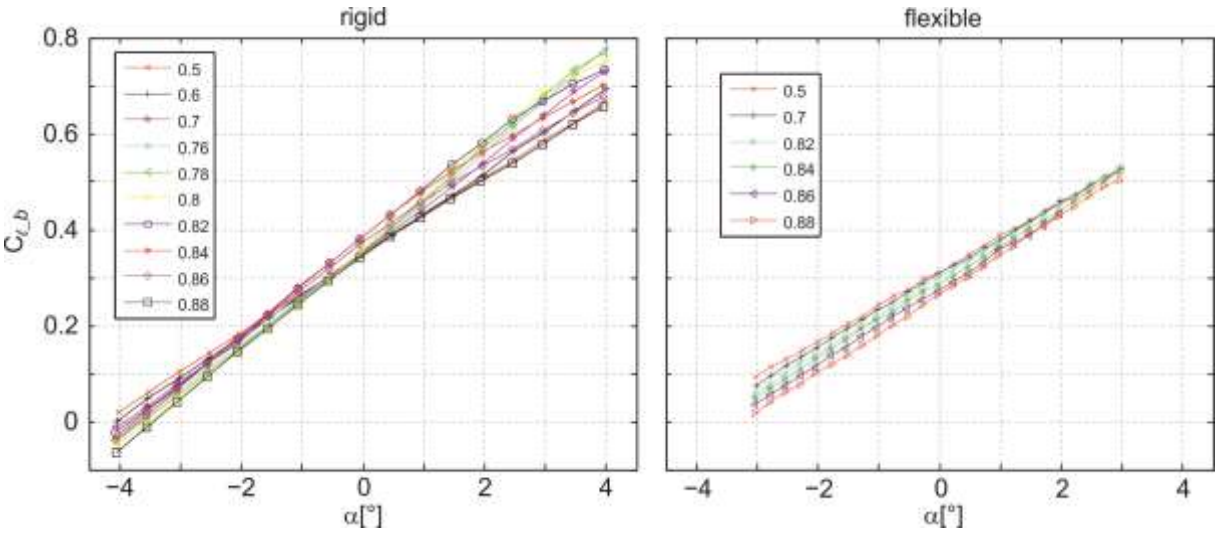

Figure 5. Global lift coefficient for the rigid wing A (left) and flexible wing B (right) depending on α and the Mach No (Reynolds numbers Re ≈ 1.3e6).

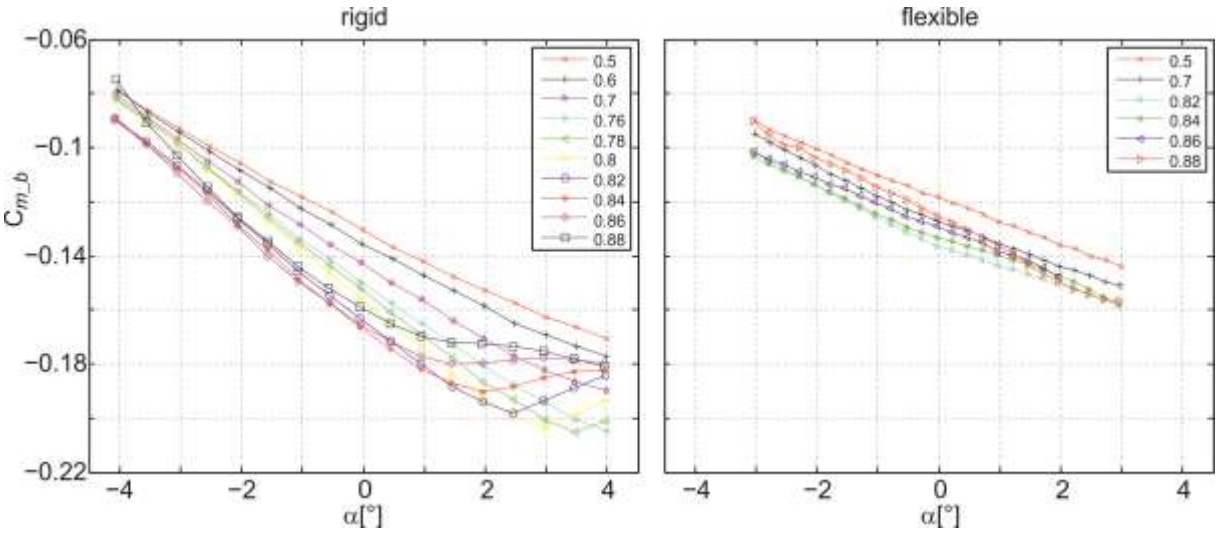

Figure 6. Global moment coefficient for the rigid-(left) and flexible wing (right) depending on α and the Mach No (Reynolds numbers Re ≈ 1.3e6) .

In **Figure 6** there is a corresponding comparison of the moment coefficient for the rigid and the flexible model. For this case it is obvious that for the rigid wing the curves become strongly curved when the Mach No is increasing and that an overall slope cannot be determined. Considering the moment curves of the flexible wing (right figure) also here the curves seem to be more straight and the variation of the slopes is less than in the case of the rigid wing, beginning at Ma = 0.82 the curve exhibit a slight S-form.
These details can better be seen in the following Figures 7.- 11.

Based on the same data in **Figure 7** a direct comparison is made for the global lift coefficient for the rigid wing (solid curve) and the flexible wing (dotted) depending on Mach No (0.5 – 0.88) and at Reynolds number around Re = 1.3e6. In order to improve the visibility the parameter angle of attack is displayed only in steps of 1° between -3° < α < 3°. For the rigid wing and positive α we see the typical behaviour, with increasing Mach number there is a slight increase of the lift coefficient up to a maximum in the transonic region, the maximum is at about Ma = 0.8 and it is shifted to 0.84 when α is decreased. For Mach numbers approaching the highest values of Ma = 0.88 the lift coefficient decreases. This behaviour can also be observed in case of 2D wings with the exception that the maximum of the lift coefficient is at around Ma = 0.75.
The formation of a maximum in the transonic regime is also obvious for the negative angles of incidence.
Considering the corresponding curves for the flexible wing, we can state that the lift is generally smaller and that in all curves there is no maximum in the transonic range. On the contrary in all curves the lift coefficient is more or less decreasing with increasing Ma, but beginning at about Ma = 0.82 the decrease is a little bit steeper.
In **Figure 8** there is the corresponding measurement of the global moment coefficient for the rigid and the flexible wing depending on Mach No. The curves c_{m_b}(Ma) for the rigid wing exhibit nearly the inverse behaviour of the corresponding c_{l_b}(Ma). There is a decrease of c_m up to a minimum in the transonic region, the minimum is at about Ma = 0.8 and it is shifted to 0.84 when α is decreased. For Mach numbers approaching the highest values of Ma = 0.88 the moment coefficient increases again up to subsonic values.
Considering the corresponding curves for the flexible wing, we can state that the moment coefficient is generally less negative in particular at higher α. In all curves the moment coefficient is slightly decreasing with increasing Ma, but beginning at about Ma = 0.82 the values increase again up to Ma = 0.88 forming a weak minimum.
The minimum is less pronounced for the highest α = 3°.
As can be expected the differences in c_{m_b}(Ma) and c_{l_b}(Ma) for both wings are very small when the lift is small as in case of α = -3° and vice versa. The reason is the fact that the deformation effects of the flexible wing are increasing in proportion to lift force.
For the flexible wing **Figures 9** and **10** deliver an impression of the influence of mass ratio or the Reynolds number on lift and moment coefficient depending on Mach No.
For every corresponding Mach number the tunnel pressure was decreased by about 30% leading to a Reynolds number around Re = 1.e6 (solid curves). The case Re = 1.3e6 (dotted curves) was taken from the foregoing figures. Again the angle of attack was varied in steps of 1° between -3° < α < 3°. The increased mass ratio μ is coupled with reduced deformation, thus the shape of the curves approach more or less the shape of the rigid wing. This effect is particularly obvious regarding the moment curve in Figure 8, where the decrease with increasing Ma and the subsequent formation of minima are more pronounced as in case of the lower mass ratio at Re = 1.3e6.

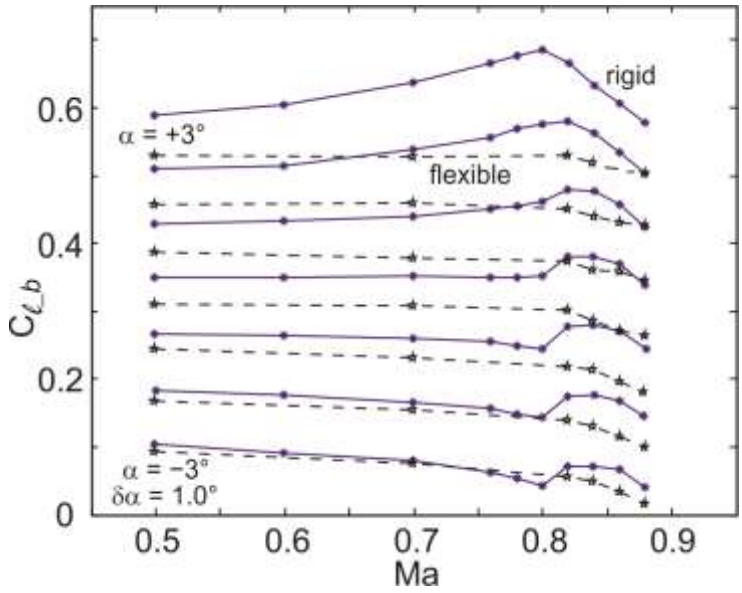

Figure 7. Comparison of the global lift coefficient for the rigid wing (solid curve) and the flexible wing (dotted) depending on Mach No (0.5 – 0.88) and at Reynolds number around Re = 1.3e6. The angle of attack was varied in steps of 1° between -3° < α < 3°.

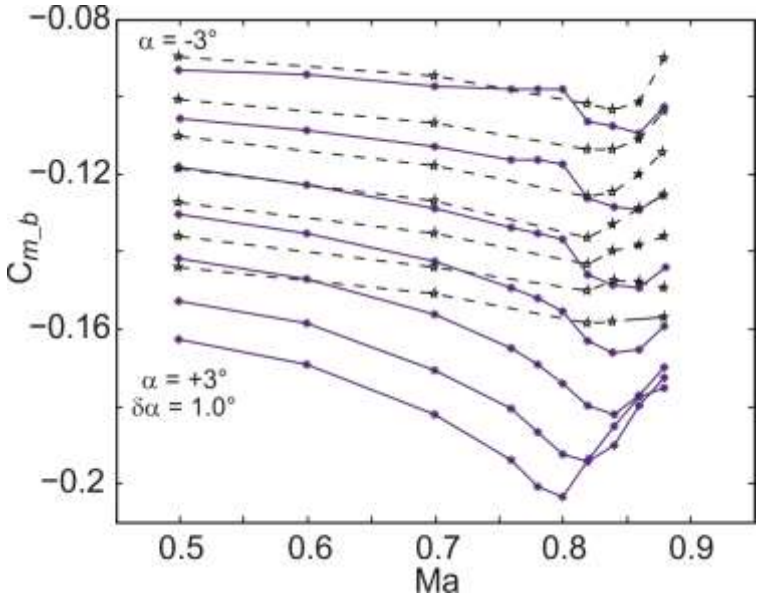

Figure 8. Comparison of the global moment coefficient for the rigid (solid curve) and the flexible wing (dotted) depending on Mach No (0.5 – 0.88) and Re = 1.3e6. The angle of attack was varied in steps of 1° between -3° < α < 3°.

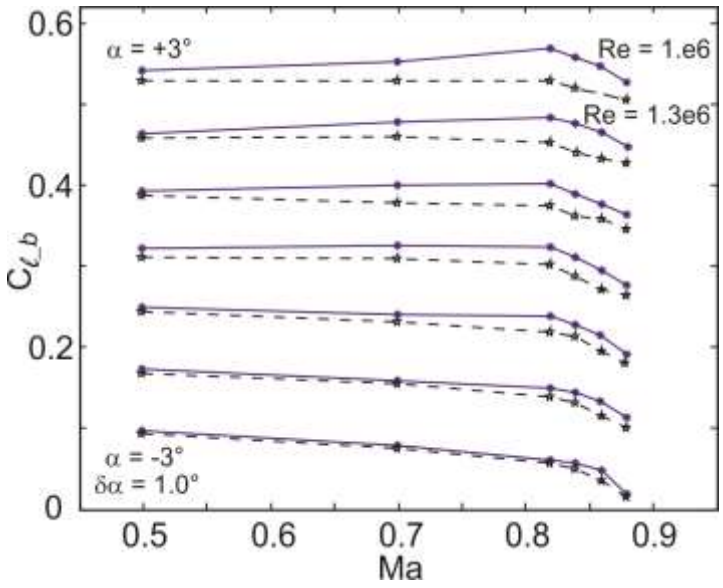

Figure 9. Global lift coefficient for the flexible wing depending on Mach No at two Reynolds numbers Re = 1.e6 (solid curves) and Re = 1.3e6 (dotted curves) . The angle of attack was varied in steps of 1° between -3° < α < 3°.

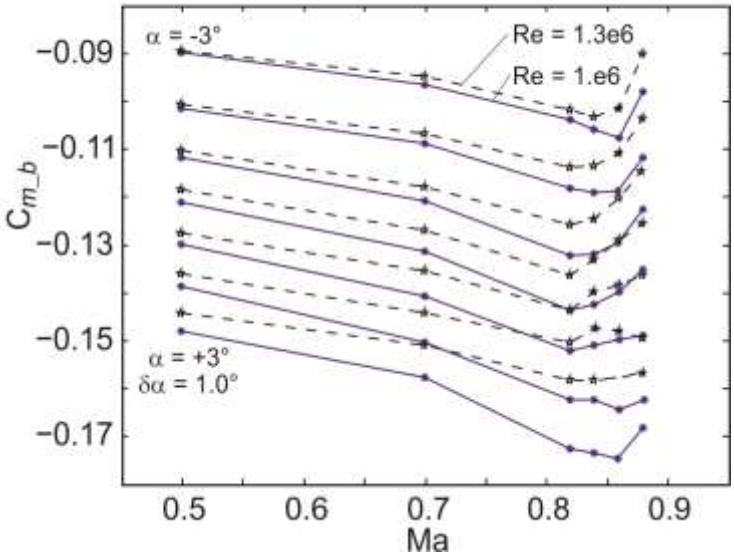

Figure 10. Global moment coefficient for the flexible wing depending on Mach No at two Reynolds numbers Re = 1.e6 (solid curves) and Re = 1.3e6 (dotted curves) . The angle of attack was varied in steps of 1° between -3° < α < 3°.

3.2 Derivatives

The derivatives of the lift and moment coefficient depending on angle of incidence are of great significance not only from an aeroelastic point of view. If there are nonlinearities in the curves, then these properties are reflected in the derivatives taken at corresponding angles of reference α_0. Such nonlinearities are indeed particularly evident in the transonic regime of the moment curves in Figure 6, which are strongly curved especially at higher α. Thus in **Figure 11** the derivatives of lift (upper diagram) and moment (lower) are presented. They were determined for the rigid wing (solid curve) and the flexible wing (dotted) depending on Mach number (Re ≈ 1.3e6). The derivatives were determined at three reference angles of incidence $\alpha_0 = 1°$, 2° and 2.5°. The angle interval regarded always was $\Delta\alpha = \pm 0.5°$. Consequently the differential quotient i.e. the slope is based on 3 angles for the rigid and 5 angles for the flexible wing.

At the first glance the impression is as follows: for subsonic Mach numbers Ma = 0.5 the values of the derivatives of lift and moment of both wings at each case are rather close together. The reason is probably the lack of significant deformation effects at this small Mach number. Then with increasing Mach number we see that apart from a deviation at the end of the transonic regime, the curves of lift and moment regarding the flexible wing are rather smooth and remaining on nearly the same level. For the rigid wing however the changes in the derivatives depending on Ma are drastic, particularly in the transonic range. In addition in this case the derivatives are strongly dependent on the reference angle of incidence α_0. With increasing Mach number for the three reference angles α_0 there is a significant increase of $dc_{l\_b}/d\alpha|_{\alpha 0}$ up to a maximum in the transonic region. For $\alpha_0 = 1°$ the maximum is at about Ma = 0.8, for $\alpha_0 = 2°$ and 2.5° there is a broad maximum at Ma ≈ 0.75 - 0.8. Beyond Ma = 0.8 a drop occurs, which is abrupt for $\alpha_0 = 2.5°$, a little bit weaker for 2.0° and more smooth in case of 1°. Having in mind the nonlinearities in the moment curves in Figure 6 it can be expected that the changes in the curves of the derivatives of the moment $dc_m/d\alpha$ are more intense and manifold.

In some sense the curves exhibit also the inverse behaviour of the corresponding curve of the lift derivative, discussed before, but in the moment case the effects are more pronounced. There is a decrease up to a minimum in the transonic region. For $\alpha_0 = 1°$ and 2° the minimum is at about Ma = 0.8, for $\alpha_0 = 2.5°$ at Ma ≈ 0.78. Regarding both higher angles beyond Ma = 0.8 and 0.78 there is nearly a jump to positive values followed by a reverse to again negative values at the highest Ma = 0.88.

The curve for $\alpha_0 = 1°$ is more smooth and exhibits no zero-crossing and no reverse.

Apart from the general remarks in the beginning of the discussion of figure 9, regarding the flexible wing the following details of the curves of the derivatives should be noted. Beginning at Ma = 0.86 for $\alpha_0 = 1°$ there is an obvious increase for the lift derivative up to a value of 5, while the corresponding moment curve decreases significantly from -0.4 to -0.7. Also the curve for $\alpha_0 = 2.5°$ exhibits a decrease to -0.6 but this reduction is followed by a reverse to the previous value -0.4.

The description of these details seem to be a little bit pedantic, but we will see in Schewe & Mai (2019) that in this region of flow parameters limit cycle oscillations of the flexible wing were observed, specifically at Ma = 0.86 and for $\alpha > 2.2°$. That is also the reason that in all figures 5 -11 there is no result for $\alpha > 2.0°$ at Ma = 0.86 and Re ≈ 1.3e6. It is not reasonable to take steady measurements, when the wing is oscillating, even if the amplitudes are limited. Already here it is interesting to remark that at the higher Mach number Ma = 0.88 the situation at the aforementioned parameters was stable again. The causes will become clear, when the diagrams of stability will be discussed in Schewe & Mai (2019).

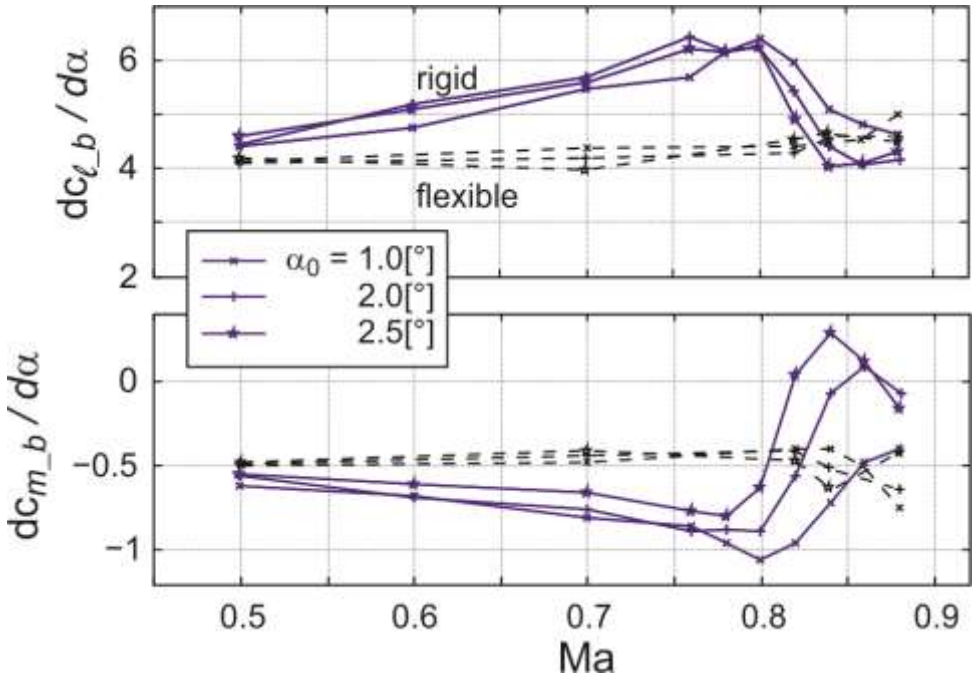

Figure 11. Comparison of the derivatives of lift (upper diagram) and moment (lower) for the rigid wing (solid curve) and the flexible wing (dotted) depending on Mach No and at Reynolds number around Re ≈ 1.3e6. The derivatives were determined at three angles of incidence α_0 = 1°, 2° and 2.5°.

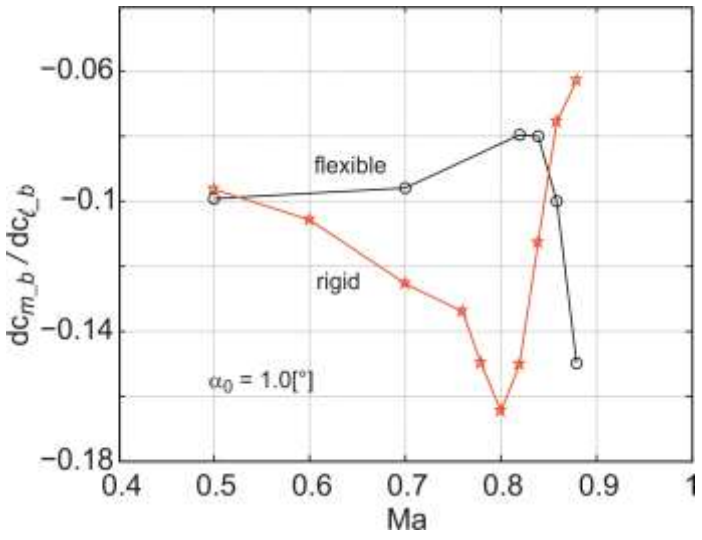

Figure 12. Comparison of the ratio of the derivatives of moment and lift for the rigid wing (solid curve) and the flexible wing (dashed) . The derivatives were determined at the reference angle of incidence α_0 = 1°.

Finally in **Figure 12** a comparison of the ratio of the derivatives of moment and lift for the rigid wing (solid curve) and the flexible wing (dotted) is shown . This value delivers information about the location of the aerodynamic center of the wing. The derivatives were determined around the angle of incidence of $\alpha_0 = 1°$.
For subsonic Mach numbers Ma = 0.5 the deformation effects are still small and consequently the values for the flexible and the rigid wing are nearly collapsing. Then with increasing Mach number the development of both curves is inverse to each other. For the elastic wing there is a moderate increase up to Ma = 0.84 followed by a rapid drop occurring at Ma = 0.88 to nearly double its previous absolute value.
For the rigid wing however there is a steep decrease ending at Ma = 0.80 followed by a rapid jump from - 0.16 in positive direction to - 0.06 , which is the value at the highest Mach number Ma = 0.88. As mentioned these changes are coupled with corresponding variations of the aerodynamic center. Comparing both curves regarding the degree of these variations, then they are considerably smaller in case of the elastic wing.

3.3 Pressure distributions

So far we have concentrated on integrated values like forces, moments and their derivatives, which reflect the influence of Mach number, angle of incidence and mass ratio on the global behaviour of both wing models under test. In the following we will present a selection of pressure distributions, taken mainly using the elastic wing. As mentioned there are three pressure sections, which will provide a deeper insight in the physical processes leading to the observed phenomena in particular in the transonic regime.
In **Figure 13** the mean pressure distributions of the three sections for Mach numbers Ma = 0.5 up to 0.88 are displayed, c is the local cord length. The angle of incidence at the root was always $\alpha = 0.96°$ and for all 6 cases the Reynolds number was adjusted to Re ≈ 1.3e6. As already shown in Figure 5 the lift coefficient measured by the balance decreases continuously from $c_{l\_b} = 0.39$ at Ma = 0.5 to $c_{l\_b} = 0.34$ at the highest Ma = 0.88. For both Ma numbers below Ma < 0.7 the pressure distributions are rather similar in all sections and the pressure coefficients are obviously not fallen below c_p^*, the critical c_p. But the suction peak behind the leading edge of the upper side touches at Ma = 0.7 the dashed line (c_p^*), thus the flow at the upper side is subsonic up to this boundary. For all Mach number Ma > 0.82 there are strong shocks around x/c ≈ 0.7 and the shock positions in the individual sections seem to be a little bit fanned out, going from the inner to the outer section the shock position moves upstream. For Ma > 0.84 at the lower side the pressures around x/c = 0.3 are fallen below the critical value.
In **Figure 14** we see pressure distributions for the three sections, depending on mass ratio μ and angle of incidence α. All measurements were taken at Ma = 0.82. In the pressure distributions in the first row, the Reynolds number had the lower value Re =1e6 and from left to right, the angles of incidence were: α = -3°, 1° and +3°. In the second row there are at corresponding angles α pressure distributions taken at the higher Reynolds number Re = 1.3e6. That means the density of the fluid and with that the aerodynamic loads were roughly 30% higher than in the case before. For the left case: α = -3°, the lift coefficient is $c_{l\_b} \approx 0$ and thus no deformation effects were to be expected. For the middle case: α = 1° , the lift coefficient is $c_{l\_b} \approx 0.4$, there we have a significant reduction of the sectional lift of the outer section by about 10%. In the right case: α = +3°, the lift coefficient is $c_l \approx 0.6$ and there are significant deformation effects evident. But first we can state, that in all sections with increasing α from 1° to 2° the first shock moves downstream, which corresponds to normal behaviour.

For α = 3° the influence of the increased density of the fluid is in particular reflected in the strong deviations of the pressure distribution of the outer section (3) when comparing with

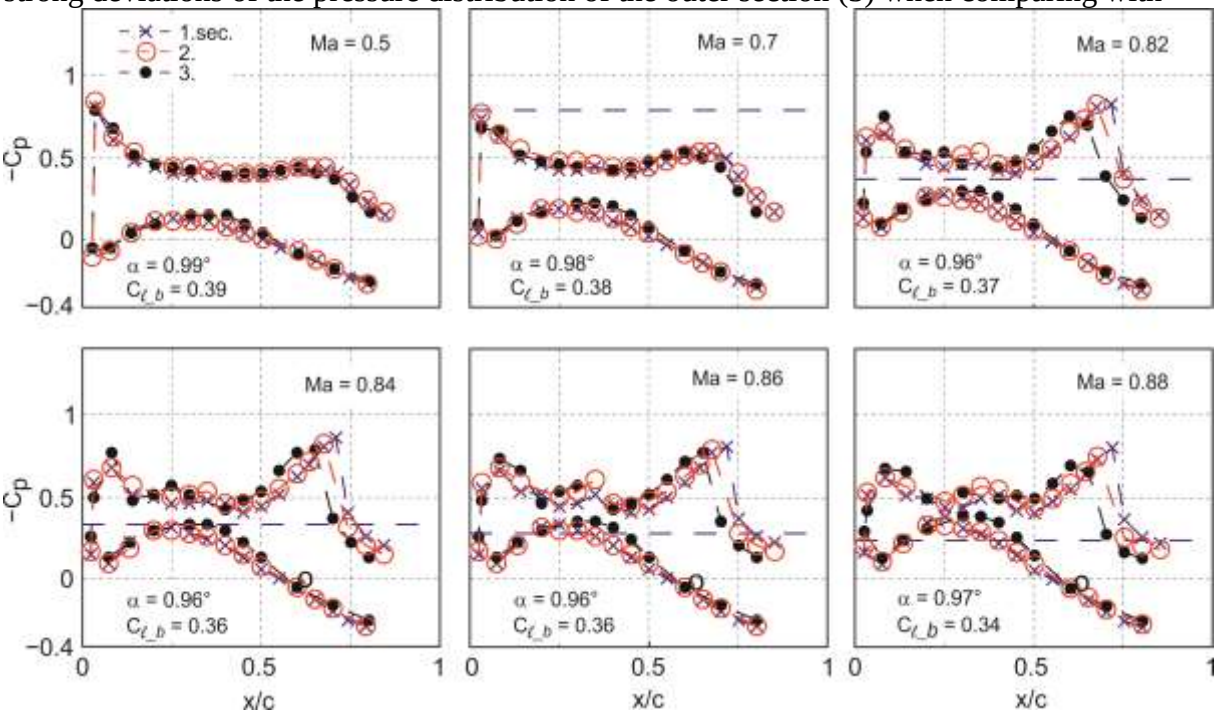

Figure 13. Pressure distributions depending on Mach No (0.5 – 0.88) at constant angle of attack α = 1.0°. The dashed line marks c_p*.

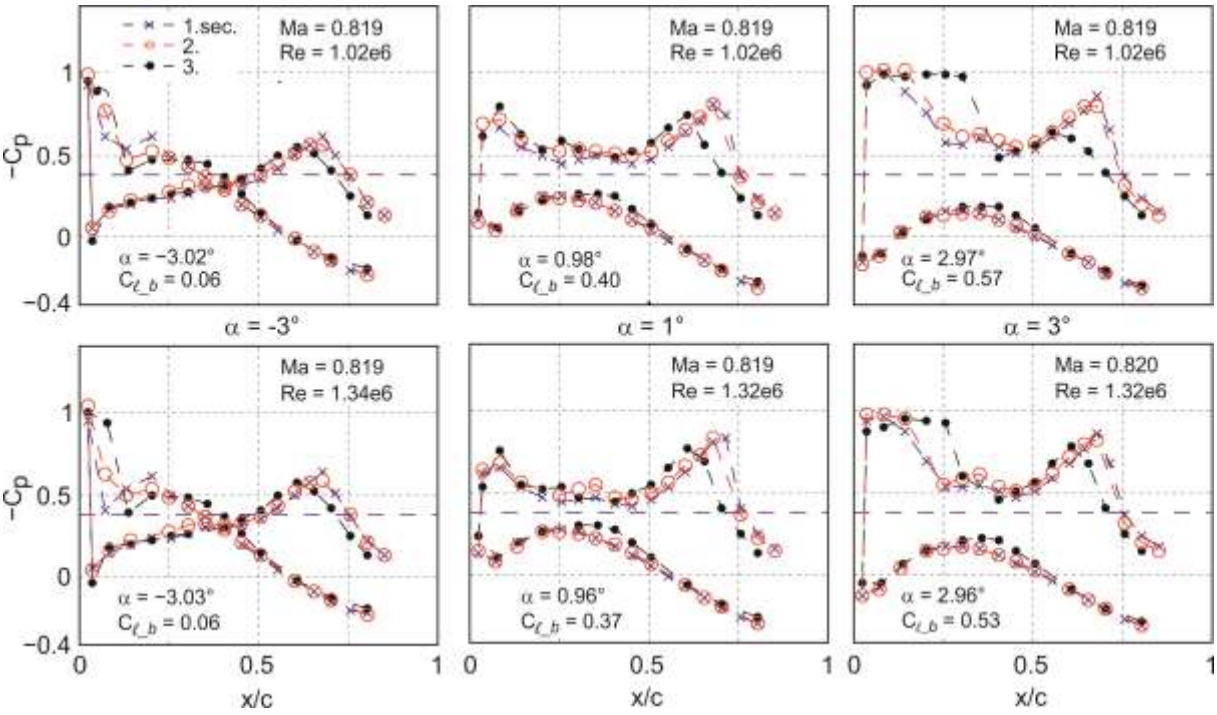

Figure 14. Pressure distributions depending on mass ratio μ and angle on incidence α (Ma = 0.82). In the first row i.e. the upper one, the Reynolds number had the lower value Re =1e6, whilst in the second row the higher case Re = 1.3e6 is displayed.

both inner sections. For the higher Reynolds number (lower mass ratio) the outer wing is retwisted leading to a strengthening of the rear shock around x/c ≈ 0.7 , the first shock however significantly has moved upstream.
Because of the significance of this phenomenon the same data for α = +3° are replotted in the next figure.

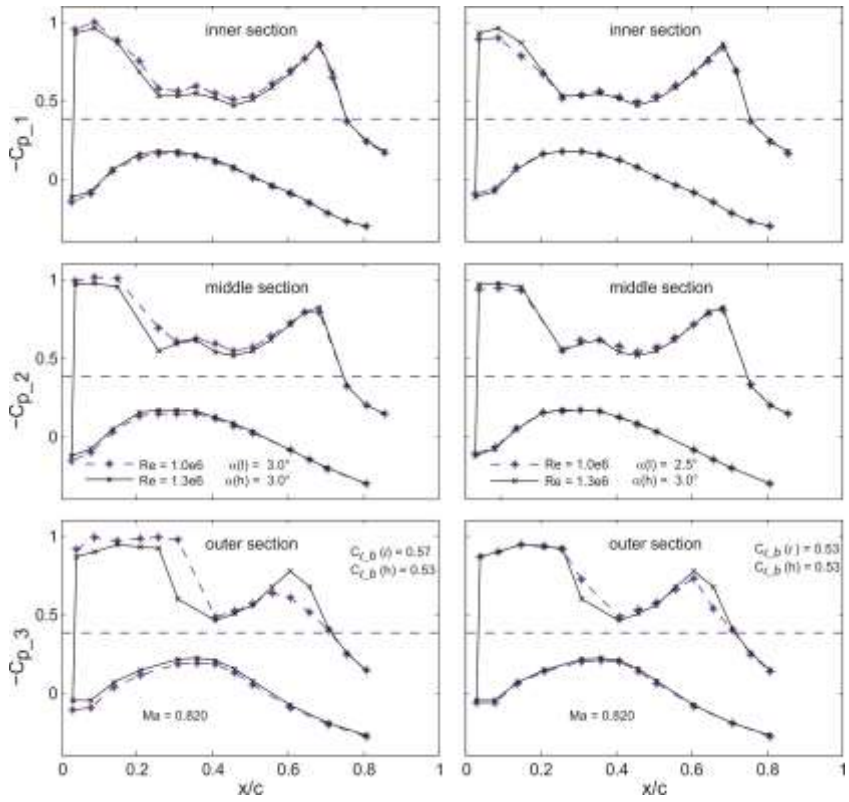

Figure 15. Deformations of the wing caused by the increase of pressure (i.e. ΔRe = + 0.3e6 corresponding Δμ). In both columns the symbol * , connected by a dashed blue line represents the lower and the symbol x (solid line) the higher pressure.

In the first column of **Figure 15** the pressure distributions for the individual sections are directly compared, when α at the root is α = const = 3°, the low Re is indicated by stars and dashed lines, while the high Re by crosses and solid lines, respectively.
For the higher stagnation pressure Δp↑ the re-twist of the wing corresponds to a reduction of the local angle of incidence (Δα↓). Consequently in all three cases for the higher loads the first shock moves upstream, a little bit at the inner section and a little bit more at the middle section while the rear shock remains nearly unchanged. In the outer section the front shock moves upstream drastically and the rear shock goes up.
As mentioned in the introduction the causing deformation phenomenon is called "Structural washout effect", i.e. the reduction of angle of incidence of a streamwise segment when the pressure is increased (Jordan (1946), Bendiksen 2009). In the following we will demonstrate that these deformation effects can be compensated by reduction of the angle of incidence at the root of Δα = -0.5°.
For this reason in the right column of Figure 15 there are again the same higher pressure measurements marked with crosses (solid line). In contrast to the lower load case of the left column (stars, dashed line) a similar case was used for the comparison which was taken also

at lower pressure but with a slightly lower angle α at the root with Δα = -0.5°. The result is that the global lift(balance) is the same for both cases $c_l(h) = c_l(l) = 0.53$ and as can be expected also the three pressure distributions are nearly the same. Thus the deformation effects caused by reduced pressure (stars, dashed blue line), which have led to a small increase of α, particularly of the outer wing are compensated by a small reduction of α at the root. We will see in Schewe & Mai (2019) that these deformation phenomena are responsible for the effect which is called "high altitude flutter" by Bendiksen (2009).

Apart from the mean pressures $c_p(x/c)$ also the RMS-pressures $c_{p\_3}(x/c,t)$ are of great interest, as they provide a measure of the intensity of the underlying process. Hence in **Figure 16** there are examples of distributions of RMS-pressures in comparison with mean pressures for the outer section (3). The selected cases correspond to the lower row of Figure 14 and partly of Figure 15 (case α = + 3°) i.e. Mach number Ma = 0.82, three angles of incidence for α = -3°, 1°, 3° and Re = 1.3e6.

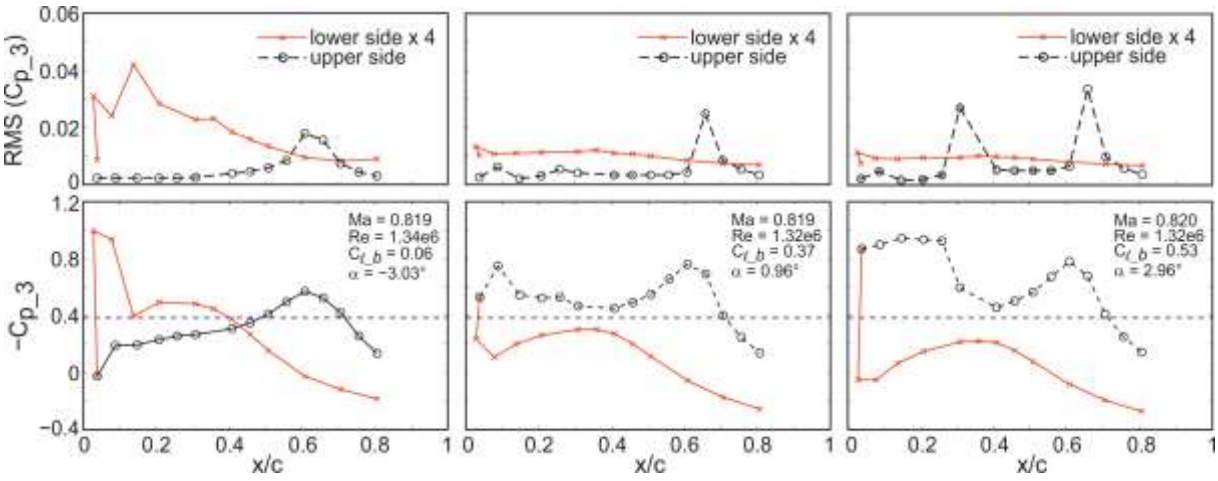

α = -3° α = 1° α = 3°

Figure 16. Distribution of RMS-pressures in comparison with mean pressures for the outer pressure section. The angle of incidence α is varied at constant Ma = 0.82. The scale of the RMS of the upper side (dotted) is the left ordinate, while the right one corresponds to the scale of the RMS of the lower side (solid), which is spread by a factor of 4.

In order to make comparisons with corresponding RMS pressures easier, in the lower row of **Figure 16** the corresponding mean pressures from Figure 14 are replotted. As the intensities of the pressure fluctuations at the lower side are significantly smaller, the scale of the RMS of the lower side is spread by a factor of 4. In particular for α = 1° and 3° the RMS at the upper side has sharp peaks at the location of the shocks with values up to 0.04, while the RMS values at the lower side are nearly constant at low values around 0.001. Only for α = - 3° there is a shock shortly behind the leading edge of the lower side, causing a RMS of about 0.01.

3.4 Transition from double shock to single shock at transonic Mach No

In the pressure distribution presented so far, we saw at higher angles of attack always double shock systems on the upper side. Then the question arises, if there is a transition from double shock to single shock and if yes, at which Mach number or at which angle of attack such a

transition would occur. A further point concerns the question, if also the rigid wing exhibits double shock systems.
For this reason **Figure 17** (left) shows pressure distributions as function of the Mach No (0.82 – 0.88), which were taken at constant α = 3.0°. The corresponding global forces and moments are already plotted in the Figures 7-8, they are the last four measuring points in the transonic regime connected by the solid line (Re ≈ 1.0e6).
Considering the shock motion from Ma = 0.82 to 0.84 it is evident that the first shock moves downstream and the second one upstream, in other words the trend is such a way that the shocks are moving against each other. Between Ma = 0.84 and 0.86 there probably occurs a merger to a single shock, which is fully developed in the pressure distribution for Ma = 0.86. In the last step at the highest Mach number Ma = 0.88 there is a steepening of the single shock and the pressures for x/c > 0.7 indicate increased separation for the upper side.
In the right **Figure 17** there are the pressure distributions as function of four angles of attack approaching α = 3.0°, taken at constant Mach number Ma = 0.86. Also for this case the corresponding global forces and moments can be found in the Figures 9-10, they are respectively the second last measuring point in the corresponding solid line (Re ≈ 1.0e6). With increasing angle of attack we have a similar development as in case of increasing Mach number. Both shocks are moving against each other and at α = 3° the merger has occurred. Considering especially the locations of the second shock then it is obviously an inverse shock motion.
As mentioned at the begin of the chapter the question arose, if also the rigid wing exhibits double shock systems. Thus a comparison with the stiff model was performed. A test case taken at the same flow parameters, Mach number Ma = 0.82, angle of incidence at the root α = 3° and a Reynolds number of Re = 1.3e6 was selected as shown in **Figure 18**. Obviously the pressure distributions are quite different. For the flexible model there is a double shock system and the second shock is located around x/c = 0.7 while in the case of the stiff model a single shock is about Δx/c = 0.1 more downstream. In addition the strength of the latter single shock is less than the second shock of the flexible wing. The global lift, measured by the balance, is significantly higher for the rigid wing with c_{l_b}(stiff) = 0.67 to c_{l_b}(flexible) = 0.53, the ratio amounts to c_{l_b}(stiff) / c_{l_b}(flexible) = 1.26, this effect is also obvious when comparing the areas between the corresponding curves in the pressure distributions.

In **Figure 19** pressure distributions depending on α are presented, which were taken using the stiff wing. The quality of the pressure measurement, reflected in the superimposed scatter, is not as high as it should be; nevertheless the tendencies and phenomena are clear.
Obviously there is no double shock at any α, but it can be stated a drastic inverse shock motion as the shock moves upstream with increasing α, this effect is probably caused by flow separation behind the shock.

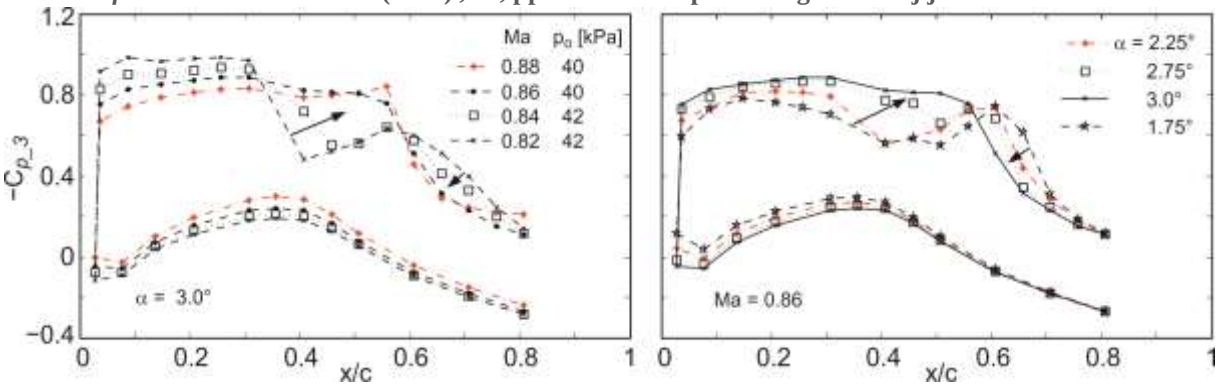

Figure 17. Transition from double shock to single shock at transonic Mach No. (Re ≈ 1.0e6) Left Figure: Pressure distributions depending on Mach No (0.82 – 0.88) at constant α = 3.0°. Right Figure: Here pressure distributions at constant Mach Ma = 0.86 for four angles of attack approaching α = 3.0°. (Cp* = - 0.28)

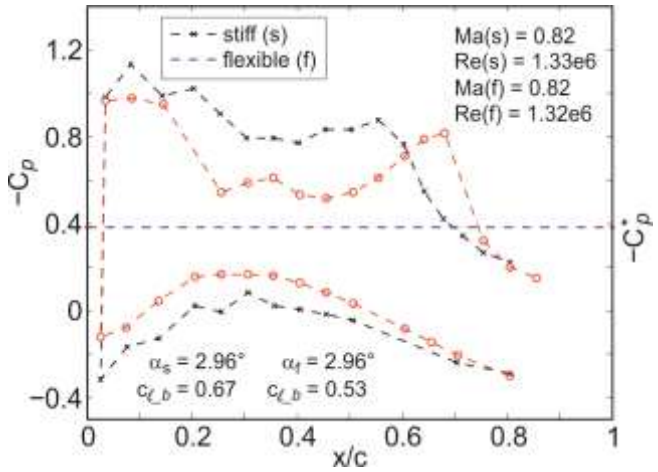

Figure 18. Comparison of pressure distributions between the flexible-(f) and stiff wing(s) at the same flow parameters. The geometrical properties of both wing are the same. For the flexible wing the 2nd pressure section was selected.

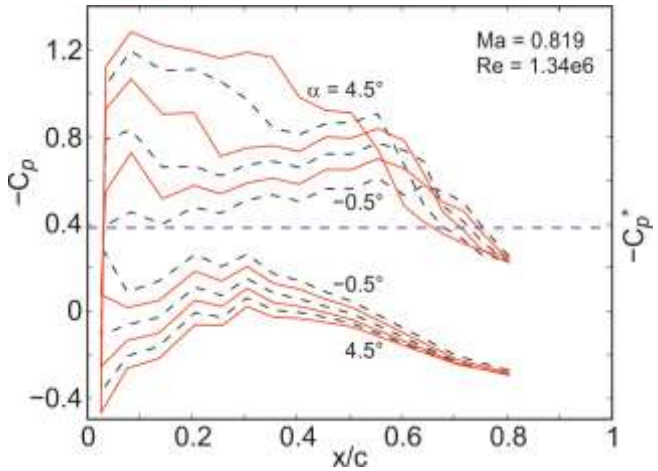

Figure 19. Pressure distributions of the stiff wing, with α as parameter (Δα = 1°). In order to make the curves more discriminable, they are alternating dotted and solid, respectively. There is no double shock at any α, but there is inverse shock motion obvious.

4 Discussion

As mentioned in the introduction the Aerostabil measurements were used by Stickan et al. (2014) as test case for their numerical simulations. It was shown that in transonic flow the pressure distributions and in particular the double shock system could be simulated only if the structural model was able to simulate a small cordwise bending of the wing section. Thus it is interesting to look for the reasons, if there is a double shock or single shock. The type of the shock system is also important because of the fact that typically a double shock system exhibits a lower wave drag than a single shock system. In Figure 17 we have seen that in the transonic regime for a small increase of the Mach number or an increase of the angle of attack α the motion of the first shock is "normal" whilst the motion of the second shock is inverse. Thus in case of a quasisteady variation of Mach number or angle of attack α both shocks are moving against each other leading to a merger at high values of Mach number or angle of attack α.

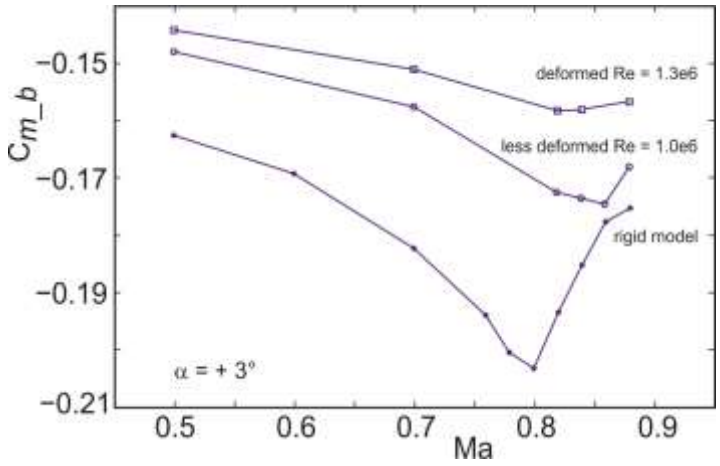

Figure 20. Global moment coefficient depending on Mach number for different states of deformation. At the root the angle of attack was α = 3°.

For the flexible wing the Figures 9 and 10 deliver an impression of the influence of mass ratio or the Reynolds number on lift and moment coefficient depending on Mach number. To illuminate the effects of elasticity in **Figure 20** two curves c_{m_b}(Ma) belonging to the flexible wing are replotted and compared with the rigid wing. The increased mass ratio by about 30% is coupled with reduced deformation. This effect is particularly obvious in the moment curve, where the decrease of c_{m_b}(Ma) with increasing Ma and the subsequent formation of minima are more pronounced as in case of the lower mass ratio at Re = 1.3e6. The shapes of the curves approach more and more the behaviour of the rigid wing, where the variations are drastic.
Considering the derivatives in Figure 10 the elastic effects are even more impressive: as mentioned because of the lack of significant deformation effects for Ma = 0.5 the derivatives of lift and moment of both wings at each case are rather close together.
Also with increasing Mach number up about Ma = 0.82 the curves of lift and moment of the flexible wing are rather smooth and remaining on nearly the same level. Then there are moderate deviations up to the end of the transonic regime.

Considering the curves of the rigid wing however the changes of the derivatives as function of Mach number are drastic, particularly in the transonic range.
In conclusion, the idea suggests itself that the elasticity – responsible for the kinematic coupling between bending and torsion - leads to a self-simplification of the entire system.

5 Conclusions

Based on our experiments regarding the influence of flexibility we have drawn the following conclusions:

- In the project "Aerostabil" the influence of the flexibility on an aeroelastically scaled swept wing was tested compared to its rigid equivalent.

- Global forces, pressure distributions etc. were analyzed, thus steady and unsteady results for the range $0.5 \leq Ma \leq 0.88$ are available.

- The angle of attack was varied from -4° to 4° and also the aeroelastic quasistatic derivatives for three reference angles were obtained.

- In the transonic regime in case of the rigid wing there is single shock, however for the flexible wing there is a double shock system

- Properties of the double shock system: for a small increase of the Mach number or an increase of the angle of attack α the motion of the first shock is "normal" whilst the motion of the second shock is inverse i.e. both shocks are moving against each other leading to a merger at high values of Mach number or angle of incidence α.

- For the flexible wing up to about Ma = 0.82 the curves of global lift, moment and derivatives are rather smooth and remaining on nearly the same level. Beyond there are moderate deviations up to the end of the transonic regime.

- Examining the corresponding curves of the rigid wing the changes are drastic, particularly in the transonic range.

Finally we can state that regarding the flexible wing the structural wash-out, particularly of the outer part leads to an attenuation of the transonic effects.

5 Acknowledgement

The authors would like to thank G. Dietz with whom we performed the experiments, his contribution is documented in Dietz et al.(2003). Further thanks go to W. Wegner and M. Braune for fruitful and stimulating discussions. The helpful support of J. Nitsche regarding data processing is also acknowledged. Further thanks go to T. Gardner for helpful suggestions and corrections regarding the manuscript.
The investigation was financially supported by the German Ministry for Education and Research and the Hermann von Helmholtz-Gemeinschaft (HGF) within the HGF-project "AEROSTABIL".

6 References

Arnold, J., Einarsson,G., Krüger,W. (2009) Multibody Simulation of an Aeroelastic

Model. NAFEMS Int. Journal of CFD case studies, Vol 8. Dec

Bendiksen, O.,O. (2009) High-Altitude Limit Cycle Flutter of Transonic Wings J. of Aircraft **46** No. 1

Bendiksen, O., O. (2011) Review of unsteady transonic aerodynamics: theory and applications. Progress in Aerospace Sciences 47.2: p. 135.

Busemann, A. (1935) Aerodynamischer Auftrieb bei Überschallgeschwindigkeit. Luftfahrtforschung Vol 12 No 6, p 210-220., Reprint in Meier, H., U. (2010)

Dietz, G. Schewe, G. Kießling, F. Sinapius, M. (2003) Limit-Cycle-Oscillation Experiments at a Transport Aircraft Wing Model. Int. Forum Aeroelasticity and Structural Dynamics (IFASD) Amsterdam

Försching, H. (2010) Aeroelasticity Problems in Compressible Subsonic and transonic Flow. Chapter in Meier, H., U. (2010) German Development of the Swept Wing: 1935-1945.

Jordan, P. (1946) Instationäre Vorgänge. in Monographien über Fortschritte der Luftfahrtforschung (seit 1939) ed. A. Betz, Band G Göttingen Monographs Concerning Progress in Germany Aeronautical Research (since 1939) , short version also in chapter 4 of Meier, H., U. (2010)

Lamarche, L., Wedemeyer, E. (1984) Minimization of wall interferences for three Dimensional models with two dimensional wall adaptation. TN 149, VKI, March

Meier, H., U. ed. (2010) German Development of the Swept Wing: 1935-1945. American Institute of Aeronautics and Astronautics.

Neumann, J., Mai, H. (2013) Gust response: Simulation of an aeroelastic experiment by a fluid–structure interaction method. Journal of Fluids and Structures, 38 , p. 290

Schewe, G. (2007) Force and Moment Measurements in Aerodynamics and Aeroelasticity using Piezoelectric Transducers. Chapter 8.2 in Springer Handbook of Experimental Fluid Mechanics

Schewe, G., Mai, H. (2019) Experiments on Transonic Limit-Cycle-Flutter of a flexible swept Wing. Journal of Fluids and Structures, 84, p.153-170

Stickan, B., Dillinger, J. and Schewe, G. (2014) Computational aeroelastic investigation of a transonic limit-cycle-oscillation experiment at a transport aircraft wing model. Journal of Fluids and Structures, 49, 223-241.

Tijdeman, H., R. Seebass, R. (1980) Transonic flow past oscillating airfoils. Annual Review of Fluid Mechanics 12.1 (1980): 181-222.

Zingel, H. et al. (1991) Measurement of steady and unsteady airloads on a stiffness scaled model of a modern transport aircraft wing. Proc. Int. Forum Aeroelasticity and Structural Dynamics (IFASD)

Schewe, Günter, and Mai, Holger. „Influence of Flexibility on the steady aeroelastic Behavior of a swept Wing in transonic Flow."
Journal of Fluids and Structures **(2018) , 81, pp. 255-269. http://doi.org/10.1016/j.jfluidstructs.2018.04.021**
DGLR 91-069, Aachen